Accessing Ultrafast Spin-Transport Dynamics in Copper Using Broadband Terahertz Spectroscopy

Jiří Jechumtál,[1,*] Reza Rouzegar,[2,3,*] Oliver Gueckstock,[2,3] Christian Denker,[4] Wolfgang Hoppe,[5] Quentin Remy,[2] Tom S. Seifert,[2,3] Peter Kubaščík,[1] Georg Woltersdorf,[5] Piet W. Brouwer,[2] Markus Münzenberg,[4] Tobias Kampfrath,[2,3] and Lukáš Nádvorník[1,†]

[1]*Faculty of Mathematics and Physics, Charles University, 121 16 Prague, Czech Republic*
[2]*Department of Physics, Freie Universität Berlin, 14195 Berlin, Germany*
[3]*Department of Physical Chemistry, Fritz Haber Institute of the Max Planck Society, 14195 Berlin, Germany*
[4]*Institut für Physik, Universität Greifswald, 17489 Greifswald, Germany*
[5]*Institut für Physik, Martin-Luther-Universität Halle, 06120 Halle, Germany*

(Received 15 October 2023; revised 31 January 2024; accepted 15 April 2024; published 30 May 2024)

We study the spatiotemporal dynamics of ultrafast electron spin transport across nanometer-thick copper layers using ultrabroadband terahertz emission spectroscopy. Our analysis of temporal delays, broadening, and attenuation of the spin-current pulse reveals ballisticlike propagation of the pulse peak, approaching the Fermi velocity, and diffusive features including a significant velocity dispersion. A comparison to the frequency-dependent Fick's law identifies the diffusion-dominated transport regime for distances > 2 nm. These findings lay the groundwork for designing future broadband spintronic devices.

DOI: 10.1103/PhysRevLett.132.226703

Following the rapid development of terahertz (THz) and antiferromagnetic spintronics [1,2], THz spin currents (TSCs) are expected to play an essential role in future ultrafast spintronic devices [3]. For example, very recently, THz-pulse-driven TSCs were used to manipulate an antiferromagnetic memory bit on subpicosecond timescales [4]. Another and complementary trigger of TSCs is optical excitation of thin-film multilayers by femtosecond laser pulses. This approach was successfully used for ultrafast spin-torque generation [5–11] or spintronic THz emission [12–20]. The latter concept has also found utility in THz investigation of formation [21–23] and dynamics [24–28] of ultrafast spin transport itself.

Following the theory works on TSCs [9,29–31], there is a rising number of experimental studies in the last years. For example, previous experiments inferred the temporal dynamics of a TSC after traversing distance d from its impact on the magnetization of an adjacent layer [5,7,8] or by optical second-harmonic generation [5,32]. Other works also addressed the spatial evolution of TSCs, i.e., the amplitude reduction of emitted THz pulses with increasing d, and deduced the relaxation length of the underlying TSCs [23,27]. However, to reveal the complex propagation character of the ultrafast spin transport, direct experimental detection of the entire spatiotemporal evolution of the TSC dynamics, including its absolute temporal delay is required.

In this Letter, we investigate such spatiotemporal evolution of subpicosecond spin-current pulses through a thin copper layer of thickness d using time-domain THz emission spectroscopy with a high temporal resolution of 40 fs. By analyzing the THz signals, we directly infer the propagation speed of TSC pulses, their broadening and attenuation with d. We observe a ballisticlike propagation of the leading edge and peak of the TSC pulse with a speed approaching the Fermi velocity of Cu. The TSC pulse duration is found to increase by a factor > 1.5 over a distance of $d = 8$ nm. Using a simple model based on a frequency-dependent Fick's law, we extract intrinsic spin-transport parameters, identify the dispersion of propagation velocities due to electron scattering as the source of the TSC pulse broadening and reveal diffusion as dominant spin-transport regime for $d > 2$ nm.

Our general approach to the generation, propagation and detection of a TSC is shown in Fig. 1. The sample is a $F|X|N$ trilayer [15] where $F = \mathrm{CoFeB}$ is a ferromagnetic thin film, $N = \mathrm{Pt}$ is a heavy metal with a large spin-Hall angle θ_{SH}, and $X = \mathrm{Cu}(d)$ is the interlayer with thickness d. First, a femtosecond laser pulse excites the $F|\mathrm{Cu}(d)|N$ sample and deposits the fraction A_F^d of the incident pump-pulse energy in F. It generates an ultrafast spin voltage $\mu_{\mathrm{s}}^d(t)$ in F [21]. As a consequence, a subpicosecond spin-current pulse $j_{\mathrm{s}}(z = 0, t)$ is launched from F into the intermediate Cu layer [21], where z is the out-of-plane coordinate (Fig. 1) and t is time. The amplitude of $\mu_{\mathrm{s}}^d(t)$ is assumed to scale with A_F^d and the corresponding normalized dynamics $\mu_{\mathrm{s}}(t) = \mu_{\mathrm{s}}^d(t)/A_F^d$ to be d independent. Second, the spin current propagates inside the X layer and undergoes attenuation and dispersion. We assume the propagation of the TSC proceeds in the linear-response regime and, thus, can be described inside X by the convolution relation [33]

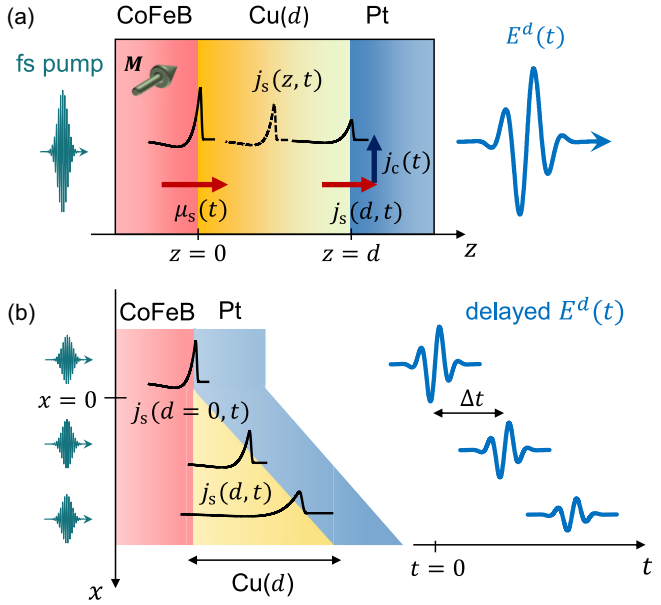

FIG. 1. THz spin-current generation, propagation, and detection in a trilayer $F|\mathrm{Cu}(d)|\mathrm{Pt}$. (a) A fs laser pulse excites a ferromagnetic layer ($F=$ CoFeB, in-plane magnetization $\boldsymbol{M}$, green arrow) and injects a spin-current pulse $j_s(z=0,t)$ (red arrow) into an intermediate layer Cu with thickness d, where it undergoes attenuation and dispersion. Finally, j_s is converted into a transverse charge current $j_c(t)$ in the Pt detection layer by the inverse spin Hall effect and radiates a THz pulse with electric field $E^d(t)$. (b) Sketch of the wedge design of the sample, showing the delayed, attenuated, and broadened signals $j_s(d,t)$ and $E^d(t)$ for different d as selected by the lateral position x of the pump focus.

$$j_s(z,t)=(\mu_s * P)(t)=\int \mathrm{d}t'\mu_s(t')P(z,t-t'). \quad (1)$$

Here, the response function $P(z,t)$ is the spin-current density that would be obtained for a $\delta(t)$-like spin voltage. Third, the current $j_s(z=d,t)$ arriving at the Pt detection layer is converted into a total transverse charge current $j_c(t)\propto\theta_{\mathrm{SH}}j_s(d,t)$ via the inverse spin Hall effect. We choose $N=$ Pt because its large inverse spin Hall effect dominates all other spin-to-charge-current conversion processes in the system [34–36]. Finally, the $j_c(t)$ emits a THz pulse with the electric field

$$E^d(t)=eZ^dA_F^dj_c(t)\propto Z^dA_F^dj_s(z=d,t), \quad (2)$$

which is detected. Here, Z^d is the frequency-independent impedance of the sample. By measuring $E^d(t)$ for $d=0$, we obtain $\mu_s(t)$ from Eqs. (2) and (1). By increasing d, one can approximately reconstruct $j_s(z=d,t)$ in the Cu spacer.

We summarize that our interpretation of the evolution of j_s using Eqs. (1) and (2) relies on the following assumptions: (i) $j_s(z=0,t)$ originates solely from $\mu_s^d(t)$ in F [33]. (ii) Its amplitude scales with A_F^d [21,34,37]. (iii) The presence of the Cu layer does not change the dynamics of $\mu_s(t)$ in F [see Supplemental Material [38], Fig. S1]. (iv) $j_s(d,t)$ is fully absorbed and converted inside N [37]. (v) The measured $j_c(t)$ is exclusively due to spin-charge conversion in $N=$ Pt, i.e., $\theta_{\mathrm{SH}}\neq 0$ only inside N [24,34]. It follows that the values of Z^d and A_F^d impact only the amplitude of $j_s(d,t)$, not its dynamics.

In the experiment, we measure an electro-optical THz signal that is related to $E^d(t)$ by the convolution relation

$$S^d(t)=(H * E^d)(t). \quad (3)$$

Here, $H(t)$ is the setup transfer function that can be determined experimentally [49,50]. Using Eq. (3), $E^d(t)$ is retrieved by the deconvolution procedure detailed in Supplemental Note 1[38] and [24,25].

Our $F|\mathrm{Cu}|N$ stack has the layer structure $\mathrm{Co_{40}Fe_{40}B_{20}}$ (2 nm)$|\mathrm{Cu}(d)|$Pt(2 nm) and is grown by electron-beam evaporation on a double-side polished $\mathrm{Al_2O_3}$ substrate [Fig. 1(a)]. On half the sample area, the Cu layer forms a wedge with a gradient of $\partial d/\partial x=3.1$ nm/mm along the x direction [Fig. 1(b)] (see Supplemental Note 2 [38] for details). This configuration allows us to conveniently select $d(x)$ in the range between 0 and 7.5 nm by positioning the pump laser beam at the appropriate position x. The other part of the sample lacks the wedge ($d=0$) and forms a stripe of $F|N$ used for referencing.

To access relative amplitudes of $j_s(z,t)$ in Eq. (2), the sample is characterized for all d in terms of the absorbed pump-pulse energy fraction A_F^d in F and the total impedance Z^d using THz transmission spectroscopy [both detailed in Supplemental Note 3 [38]]. The measured Z^d are found to be almost frequency independent up to 7 THz for all d [Fig. S2(b) and (c) [38]] and decrease steeply with d [Fig. S2(d) [38]]. For $d=11$ nm, the stack conductance G is dominated by the Cu layer (Supplemental Note 3 [38]) and, thus, the Drude model [50,51] $G(\omega)\propto 1/(1-\mathrm{i}\omega\tau)$ can be used to estimate the electron scattering time τ in Cu. Indeed, it provides a good fit to the data for $1<\tau<10$ fs [Fig. S2(f) [38]]. This τ is much smaller than the several tens of fs typical for epitaxial Cu layers [52,53] and assigned to the polycrystalline nature of our evaporation-deposited wedge.

In the THz emission experiments, the sample is excited by a train of ultrashort laser pulses (wavelength 790 nm, duration 10 fs, repetition rate 80 MHz, energy per pulse 2 nJ) from a Ti:sapphire laser oscillator. The pump beam is focused to a spot with a full width at half maximum (FWHM) of the intensity of ~30 μm on the sample. Its lateral position x sets d with a precision of ~0.1 nm [Fig. 1(b)]. The magnetization $\boldsymbol{M}$ of the F layer is controlled by an external magnetic field of ~10 mT. The emitted THz electric field $E(t)$ propagates in a nitrogen atmosphere and is detected as an electrooptical (EO) signal $S(t)$ via EO

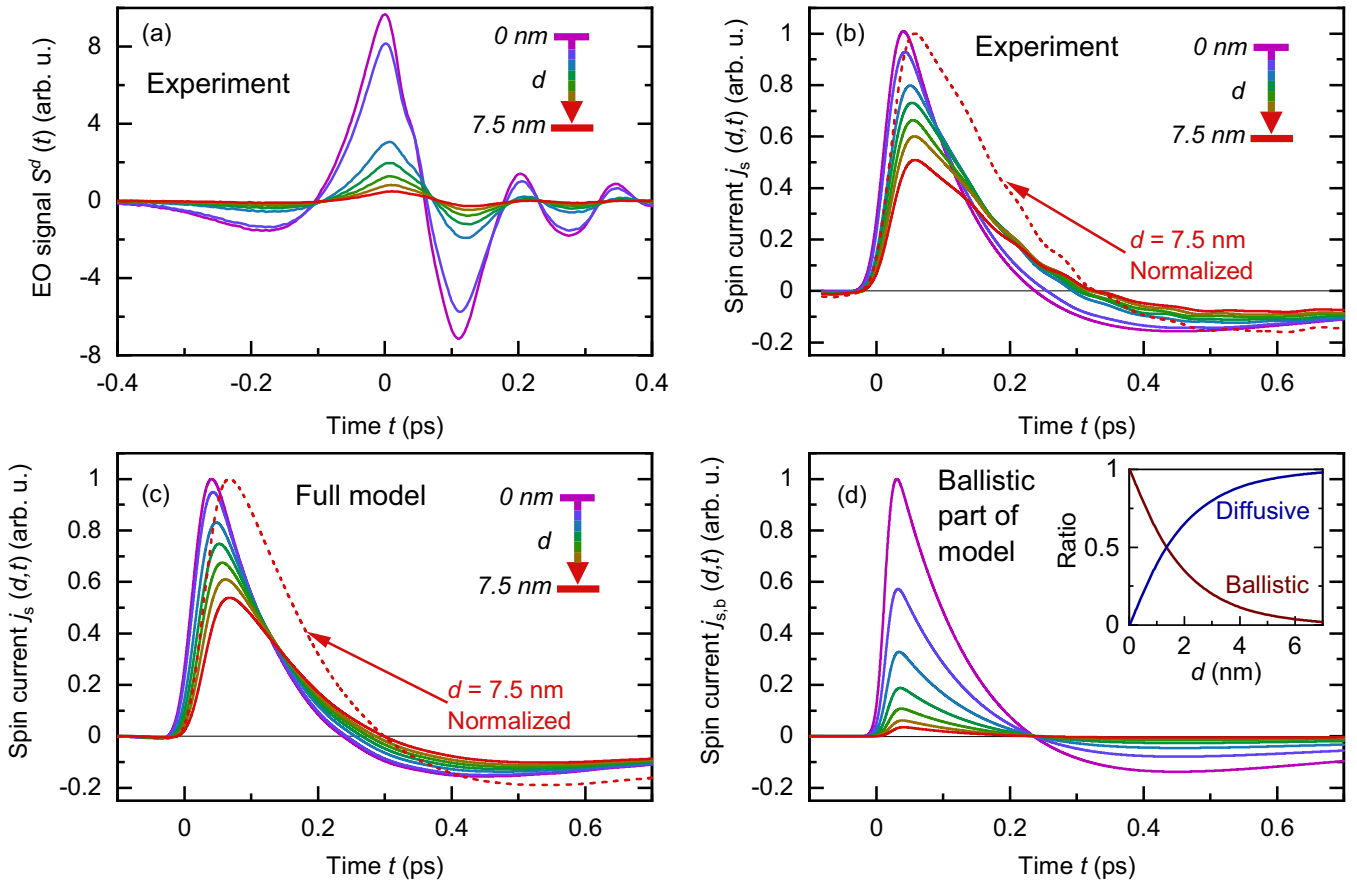

FIG. 2. THz spin currents $j_s(z,t)$ after traversing the Cu interlayer. (a) Measured THz emission signals $S^d(t)$ from $F|\mathrm{Cu}(d)|N$ stacks for $d = 0, 0.6, 2.2, 3.4, 4.7, 5.9, 7.5$ nm (color-coded). (b) Extracted spin-current dynamics $j_s(z=d,t)$ according to Eqs. (1) and (2). The dashed black arrow indicates the delay Δt of the current peak. (c) Spin currents $j_s(z=d,t)$ calculated using the spin-propagation model of Eqs. (1), (4), (6) with $v_F = 1.1$ nm/fs and $\tau = 4$ fs. (d) Calculated ballistic contribution to $j_s(z,t)$ by taking $\tau_{sf} = \tau$ in Eq. (5). Red dashed curves in (b),(c) are $j_s(z=d,t)$ for $d = 7.5$ nm with maximum normalized to unity. Inset: ratio of ballistic and diffusive components in $j_s(z,t)$ vs d.

sampling [54,55] in a 250 μm thick GaP(110) crystal by using linearly polarized probe pulses (0.6 nJ) split from the pump beam. Even though the temporal resolution of the subsequent analysis is ∼40 fs, a continuously scanning delay line together with a high signal-to-noise ratio of our setup allows us to resolve the minimal increment of time t and, thus, also the temporal delays Δt of $S(t)$, as fine as 1.6 fs.

Typical THz-emission waveforms $S^d(t)$ from the CoFeB|Cu(d)|Pt samples are shown in Fig. 2(a). As d increases from 0 to 7.5 nm, the overall signal amplitude decreases by roughly a factor of 20. The noticeable reduction between the second and third curve originates from the non-equidistant choice of d and the steep nonlinear decrease of Z^d, while the oscillatory features at $t > 0.2$ ps arise from the EO detection process (Supplemental Note 1 [38]). Interestingly, the absolute maximum and minimum of $S^d(t)$ undergo a gradual temporal shift Δt (dashed arrows), where Δt appears to be larger for the minimum. We experimentally rule out possible trivial sources of time delays in $S^d(t)$ such as the Gouy phase shift, a variation of the substrate thickness and long-term temporal drifts of the laser (see Supplemental Note 4 [38]). We note that all waveforms are antisymmetrized with respect to $\boldsymbol{M}$, i.e., $S^d(t) = [S^d(+\boldsymbol{M},t) - S^d(-\boldsymbol{M},t)]/2$, which captures only relevant effects odd in $\boldsymbol{M}$ (see Fig. S3 and Supplemental Note 5 [38] for further confirmation of the spintronic origin of signal).

To extract the TSC density $j_s(z=d,t)$ directly behind the Cu layer, we apply Eqs. (2) and (3) to $S^d(t)$ normalized by $Z^d A_F^d$ [see the mono-exponential amplitude decrease in Fig. S4 [38] as compared to Fig. 2(a)] and use assumptions (i-v) (Supplemental Note 1[38]). Figure 2(b) shows the resulting $j_s(z=d,t)$ for various values of $z = d$ and, thus, provides the approximate spatial evolution of the ultrafast dynamics of the TSCs. The rise time of $j_s(d=0,t)$ indicates that the time resolution of the extracted TSCs is ≈40 fs. Both the gradual attenuation and the rising temporal shift Δt of the THz signals $S^d(t)$ vs d are preserved in the TSCs [arrow in Fig. 2(b)]. Importantly, $j_s(d,t)$ undergoes a notable

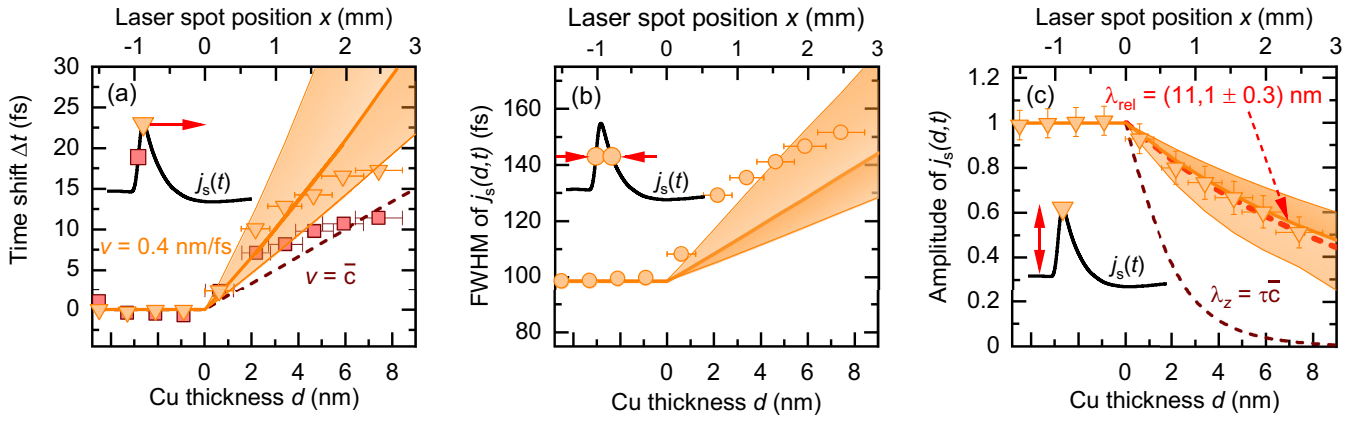

FIG. 3. Analysis of $j_s(d,t)$ from Fig. 2(b). (a) Delay Δt of the peak (orange triangles) and leading edge (red squares) of the spin current $j_s(z=d,t)$ as a function of Cu thickness d. (b) Full width at half maximum (FWHM) (circles) and (c) peak amplitude of $j_s(z=d,t)$ vs d. In all panels, results of the model with $v_F = 1.1 \pm 0.2$ nm/fs and $\tau = 4 \pm 2$ fs are shown by orange solid curves (central values) and orange shades (uncertainties). The results of the ballistic contribution are shown by dark-red dashed curves.

broadening that is clearly visible for $j_s(d=0,t)$ vs the normalized $j_s(d=7.5\ \text{nm},t)$ (red dashed line) without any further analysis. This behavior indicates that the TSC undergoes a significant dispersion.

To quantify these qualitative observations, we look at the details of the measured spin current by extracting temporal delay Δt, the full width at half maximum (FWHM), and amplitude of the spin current pulses. First, we extract Δt relative to $j_s(d=0,t)$ for the leading edge (at half maximum) and peak of the spin current for all measured d. The resulting Δt vs d [Fig. 3(a)] shows a monotonic nonlinear increase. The propagation velocity of the leading edge and peak of $j_s(d,t)$ can be obtained from fitting the mean slope of $\Delta t(d)$ [Fig. S5(a) [38]], yielding propagation speeds of, respectively, (0.6 ± 0.1) nm/fs and $\approx$0.4 nm/fs for the whole data range and, correspondingly, $\approx$1.2 and $\approx$0.7 nm/fs for $d > 2$ nm [Fig. S5(b) [38]]. The latter values are sizable and almost reach the Fermi velocity ($\sim$1.1 nm/fs [53]) of electrons in Cu. Moreover, the pulse leading edge seems to propagate faster than the subsequent pulse peak. This behavior implies a broadening of the leading edge and, possibly, the whole TSC pulse $j_s(d,t)$ as d increases.

Second, the FWHM of $j_s(d,t)$ vs d is shown in Fig. 3(b). Indeed, we find a significant pulse broadening from 100 fs at $d=0$ by a factor of 1.5 at $d=7.5$ nm of Cu. Third, the amplitude of the peak TSC decreases exponentially with d with a relaxation length of $\lambda_{rel} = (11.1 \pm 0.3)$ nm [Fig. 3(c)]. We note that the abrupt amplitude reduction visible in $S^d(t)$ around $d=2$ nm [Fig. 2(a)] disappears in amplitudes of $j_s(d,t)$ due to normalization by $Z^d A_F^d$. Therefore, the proper λ_{rel} cannot be retrieved directly from $S^d(t)$ and underscores the importance of the reconstruction of $j_s(d,t)$ [see Fig. S4(b) [38]].

To better understand the observed TSC-pulse dynamics [Figs. 2(b) and 3(a)–3(c)], in particular its edge and peak delay and temporal broadening, we make use of an analytical model of ultrafast spin transport in Cu [29,30]. It relies on two macroscopic relationships that can be derived from the Boltzmann transport equation. (i) In a generalized version of Fick's law, $j_s(z,\omega) = -D_s(\omega)\partial_z\mu_s$, the diffusion coefficient is proportional to the Cu conductance. Thus, it has the same Drude-type frequency dependence, $D_s(\omega) \propto G(\omega) \propto 1/(1-i\omega\tau)$, with τ estimated in Fig. S2(f) [38]. (ii) In the time-domain continuity equation, $\partial_z j_s \propto -\partial_t\mu_s - 2\mu_s/\tau_{sf}$, the second term is due to spin relaxation in Cu [56–59].

By combining (i) and (ii) (see Supplemental Note 6 [38]), we find that the response function P [see Eq. (1)] can be written as the Fourier integral

$$P(z,t) = \int d\omega\, e^{ik(\omega)z - i\omega t}. \tag{4}$$

Here, for each frequency $\omega/2\pi$, the associated complex-valued wave vector k is given by the dispersion relation

$$\bar{c}^2k^2 = \omega^2 + i\omega(\tau^{-1} + 2\tau_{sf}^{-1}) - 2(\tau\tau_{sf})^{-1}, \tag{5}$$

where $\bar{c} = v_F/\sqrt{3}$ is the mean electron band velocity projected on the z direction. By considering that $\tau_{sf} \gg \tau$ [56–59], this relation simplifies to

$$\frac{\bar{c}^2k^2}{\omega^2} = 1 - \frac{1}{i\omega\tau}. \tag{6}$$

Equations (4) and (6) allow us to interpret TSC-pulse propagation through Cu as signal transmission [29]. The frequency-dependent group velocity $\partial_k\omega$ and attenuation $\mathrm{Im}k(\omega)$ follow from the dispersion relation [Eq. (6)]. Note that the model captures both ballistic and diffusive transport, which prevail, respectively, for angular frequencies ω much larger and smaller than the rate τ^{-1} of electron momentum scattering. For example, for $\omega \gg \tau^{-1}$, we can

neglect the second term on the right-hand side of Eq. (6), and the TSC-pulse group velocity approaches the mean electron band velocity $\bar{c}$.

We use Eqs. (1), (4), and (6), the experimentally given $\mu_s(t)$, and the known $v_F = 1.1$ nm/fs [53] and the mean $\tau = 4$ fs [Fig. S2(f) [38]] to calculate the resulting TSC dynamics. The calculated $j_s(z = d, t)$ [Fig. 2(c)] agree well with the measured $j_s(d, t)$ [Fig. 2(b)]. From the modeled dynamics, we extract the peak delay Δt, the pulse FWHM and peak amplitude of $j_s(z = d, t)$ as a function of d and plot them as orange lines in Fig. 3(a)–3(c). The orange shaded areas correspond to a small variation of v_F by $\pm$ 0.2 nm/fs and τ by $\pm$ 2 fs. We find reasonably good agreement of model and experiment, showing that the transport features can be explained by a combination of ballistic and diffusive components. However, we find that the model underestimates the TSC pulse broadening and has a slight mismatch with Δt.

To obtain more insight into the role of electron scattering, we extract the ballistic component $j_{s,b}(z, t)$ of the calculated $j_s(z, t)$ by considering a special condition of $\tau_{sf} = \tau = 4$ fs and employ it in the exact dispersion relation for $k(\omega)$ [Eq. (5)]. This choice spin depolarizes all electrons that have experienced a scattering event and, thus, does not make them available for diffusive spin transport. The resulting ballistic component $j_{s,b}(d, t)$ [Fig. 2(d)] decays considerably faster with increasing d than the diffusive component $j_s(z, t) - j_{s,b}(z, t)$, as also documented by the ratio of the 2 contributions [inset in Fig. 2(d)]. For comparison, the parameters Δt and attenuation of the maximum of the ballistic component are shown in Figs. 3(a) and 3(c) as dark-red dashed curves. We see that the attenuation and broadening of the measured TSC pulses cannot be explained by scattering-free spin transport and requires a nonballistic component. Indeed, the observed amplitude relaxation length of $\lambda_{rel} \sim 11$ nm is about 5 times larger than the mean free-path of $\lambda_z = \bar{c}\tau \approx 2$ nm along z. Figures 2(d) and 3(c) also highlight that the diffusion (scattering-based) transport modes dominate the propagation for $d > 2$ nm.

Interestingly, the propagation speed of the TSC pulse front or its peak still reaches values close to v_F and almost matches the wave-front velocity $\bar{c}$ expected from the model. This observation indicates that the leading parts of the TSC pulse are formed by electrons that experience only a few collisions, allowing for ultrafast (ballisticlike) spin propagation over length scales of more than 10 nm, not strictly limited by λ_z. To directly observe modes propagating at the speed v_F, it would be necessary to fulfill $\omega > 1/\tau$ by using materials with significantly larger τ, or by increasing the bandwidth of our experiment.

The role of the particular spin-transport regime or different layer quality, i.e., different τ, is manifested in the literature by an interestingly large variation of λ_{rel} for the spin transport in Cu: ranging from 4 [37], through 11 [60] and 50 [27], up to 120 nm [8] in the ultrafast transport experiments, and even larger values of the order of hundreds of nm are reported at GHz and lower frequencies [27,57,61]. It can be understood within the theory in Refs. [29,30] which shows that the diffusive spin transport, observed in the limit of $\omega \sim 0$, becomes ballistic when $\omega\tau \gg 1$. The ballistic spin transport by conduction electrons is limited by the mean free path at which, statistically, the first scattering event occurs. On the other hand, the diffusive spin transport allows for a further random-walk-like transport which extends to the usually significantly larger spin diffusion length [62]. While the low frequency spin transport is of the diffusive nature, the ultrafast and THz experiments study broadband spin-current pulses and, thus, the measured spin-current decay length reflects an average λ_{rel}, ranging between the mean free path and the spin diffusion length.

The source of the visible underestimate of the TSC pulse broadening by the used model [Fig. 3(b)] could lie in disregarding a possible initial velocity distribution at $t = 0$. Indeed, the varying z component of the initial velocity $v_z = v_F \cos\theta$ of electrons moving at angle θ from the out-of-plane z axis might also induce an effective velocity distribution, not included in the model, and it can lead to an additional broadening of $j_s(z = d, t)$ [5,63]. However, if we apply the ballistic-only model with a homogeneous initial distribution of θ described in methods in Ref. [63], it would induce a broadening by only a factor of ~1.2 over 8 nm of Cu, i.e., a significantly smaller value than what was observed in the measured dynamics. In order to include a more realistic initial v_z distribution in the model, one would need to analyze the orbital symmetry matching between CoFeB and Cu. Because of these limitations, the model does not capture the slightly nonlinear trend in Figs. 3(a) and 3(b) for $d < 3$ nm and, thus, invites detailed studies of $\mu_s(t)$ at extreme interlayer thicknesses.

In summary, we employed time-domain THz emission spectroscopy to directly measure the spatial and temporal evolution of ultrafast spin currents triggered by optical excitation of metallic thin films. The observed temporal delays, significant broadening, and attenuation of TSCs for varying Cu spacer thickness indicate diffusion-dominated spin transport and related dispersion of TSCs. A simple model based on the dynamic diffusion equation explains very well our data by assuming realistic values $v_F = 1.1$ nm/fs and $\tau = 4$ fs. If confirms the dominant role of electron-scattering in TSCs for thicknesses $d > 2$ nm. Notably, the analysis of the TSC pulse front revealed that the spin-current speed approaches the Fermi velocity. Our methodology facilitates practical implementation of spin currents in ultrafast spintronic devices. For spintronic emitters [13–16], we anticipate that Cu intermediate layers can be used to tune the spin current profile and consequently the performance of the spintronic THz emission.

The authors thank Afnan Alostaz for help with measurements. The authors acknowledge funding by the Czech Science Foundation through projects GA CR (Grant No. 21–28876J), the Grant Agency of the Charles University (SVV–2024–260720), the Deutsche Forschungsgemeinschaft (DFG, German Research Foundation) through the Collaborative Research Center SFB TRR 227 "Ultrafast spin dynamics" (project ID 328545488, projects A05, B02, and B03), and the priority program SPP2314 INTEREST (project ITISA; Grant No. KA 3305/5-1), the European Research Council (ERC) through the H2020 CoG project TERAMAG (Grant No. 681917) and the Ministry of Education, Youth and Sports of the Czech Republic through the OP JAK call Excellent Research (TERAFIT Project No. CZ.02.01.01/00/22_008/0004594). R. R. acknowledges support by the International Max Planck Research School (IMPRS) for Elementary Processes in Physical Chemistry. J. J. acknowledges the support by the Grant Agency of the Charles University (Grant No. 120324). P. K. acknowledges the support by the Grant Agency of the Charles University (Grant No. 166123).

*These authors contributed equally to this work.
†lukas.nadvornik@matfyz.cuni.cz

[1] T. Jungwirth, X. Marti, P. Wadley, and J. Wunderlich, Antiferromagnetic spintronics, Nat. Nanotechnol. **11**, 231 (2016).
[2] P. Němec, M. Fiebig, T. Kampfrath, and A. V. Kimel, Antiferromagnetic opto-spintronics, Nat. Phys **14**, 229 (2018).
[3] M. B. Jungfleisch, W. Zhang, and A. Hoffmann, Perspectives of antiferromagnetic spintronics, Phys. Lett. A **382**, 865 (2018).
[4] Y. Behovits *et al.*, Nonlinear terahertz Néel spin-orbit torques in antiferromagnetic Mn2Au, arXiv:2305.03368.
[5] A. Melnikov, L. Brandt, N. Liebing, M. Ribow, I. Mertig, and G. Woltersdorf, Ultrafast spin transport and control of spin current pulse shape in metallic multilayers, Phys. Rev. B **106**, 104417 (2022).
[6] I. Razdolski, A. Alekhin, N. Ilin, J. P. Meyburg, V. Roddatis, D. Diesing, U. Bovensiepen, and A. Melnikov, Nanoscale interface confinement of ultrafast spin transfer torque driving non-uniform spin dynamics, Nat. Commun. **8**, 15007 (2017).
[7] A. J. Schellekens, K. C. Kuiper, R. R. J. C. de Wit, and B. Koopmans, Ultrafast spin-transfer torque driven by femtosecond pulsed-laser excitation, Nat. Commun. **5**, 4333 (2014).
[8] G.-M. Choi, B.-C. Min, K.-J. Lee, and D. G. Cahill, Spin current generated by thermally driven ultrafast demagnetization, Nat. Commun. **5**, 4334 (2014).
[9] D. Rudolf *et al.*, Ultrafast magnetization enhancement in metallic multilayers driven by superdiffusive spin current, Nat. Commun. **3**, 1037 (2012).
[10] G. Malinowski, F. Dalla Longa, J. H. H. Rietjens, P. V. Paluskar, R. Huijink, H. J. M. Swagten, and B. Koopmans, Control of speed and efficiency of ultrafast demagnetization by direct transfer of spin angular momentum, Nat. Phys. **4**, 855 (2008).
[11] L. Brandt, U. Ritzmann, N. Liebing, M. Ribow, I. Razdolski, P. Brouwer, A. Melnikov, and G. Woltersdorf, Effective exchange interaction for terahertz spin waves in iron layers, Phys. Rev. B **104**, 094415 (2021).
[12] T. Kampfrath *et al.*, Terahertz spin current pulses controlled by magnetic heterostructures, Nat. Nanotechnol. **8**, 256 (2013).
[13] T. Seifert *et al.*, Efficient metallic spintronic emitters of ultrabroadband terahertz radiation, Nat. Photonics **10**, 483 (2016).
[14] C. Bull, S. M. Hewett, R. Ji, C.-H. Lin, T. Thomson, D. M. Graham, and P. W. Nutter, Spintronic terahertz emitters: Status and prospects from a materials perspective, APL Mater. **9**, 090701 (2021).
[15] T. S. Seifert, L. Cheng, Z. Wei, T. Kampfrath, and J. Qi, Spintronic sources of ultrashort terahertz electromagnetic pulses, Appl. Phys. Lett. **120**, 180401 (2022).
[16] E. Th. Papaioannou and R. Beigang, THz spintronic emitters: A review on achievements and future challenges, Nanophotonics **10**, 1243 (2021).
[17] R. Rouzegar *et al.*, Broadband spintronic terahertz source with peak electric fields exceeding 1.5 MV/cm, Phys. Rev. Appl. **19**, 034018 (2023).
[18] O. Gueckstock, L. Nádvorník, T. S. Seifert, M. Borchert, G. Jakob, G. Schmidt, G. Woltersdorf, M. Kläui, M. Wolf, and T. Kampfrath, Modulating the polarization of broadband terahertz pulses from a spintronic emitter at rates up to 10 KHz, Optica **8**, 1013 (2021).
[19] C. Zhou *et al.*, Broadband terahertz generation via the interface inverse Rashba-Edelstein effect, Phys. Rev. Lett. **121**, 086801 (2018).
[20] T. J. Huisman, C. Ciccarelli, A. Tsukamoto, R. V. Mikhaylovskiy, Th. Rasing, and A. V. Kimel, Spin-photocurrents generated by femtosecond laser pulses in a ferrimagnetic GdFeCo/Pt bilayer, Appl. Phys. Lett. **110**, 072402 (2017).
[21] R. Rouzegar *et al.*, Laser-induced terahertz spin transport in magnetic nanostructures arises from the same force as ultrafast demagnetization, Phys. Rev. B **106**, 144427 (2022).
[22] H. Qiu *et al.*, Ultrafast spin current generated from an antiferromagnet, Nat. Phys. **17**, 388 (2021).
[23] E. Rongione *et al.*, Emission of coherent THz magnons in an antiferromagnetic insulator triggered by ultrafast spin-phonon interactions, Nat. Commun. **14**, 1818 (2023).
[24] O. Gueckstock, R. L. Seeger, T. S. Seifert, S. Auffret, S. Gambarelli, J. N. Kirchhof, K. I. Bolotin, V. Baltz, T. Kampfrath, and L. Nádvorník, Impact of gigahertz and terahertz transport regimes on spin propagation and conversion in the antiferromagnet IrMn, Appl. Phys. Lett. **120**, 062408 (2022).
[25] P. Jiménez-Cavero, O. Gueckstock, L. Nadvornik, I. Lucas, T. S. Seifert *et al.*, Transition of laser-induced terahertz spin currents from torque- to conduction-electron-mediated transport, Phys. Rev. B **105**, 184408 (2022).
[26] L. Nádvorník *et al.*, Terahertz spin-to-charge current conversion in stacks of ferromagnets and the transition-metal

dichalcogenide $NbSe_2$, Adv. Mater. Interfaces **9**, 2201675 (2022).
[27] J. Gorchon, S. Mangin, and M. Hehn, Is terahertz emission a good probe of the spin current attenuation length?, Appl. Phys. Lett. **121**, 012402 (2022).
[28] M. Meinert, B. Gliniors, O. Gueckstock, T. S. Seifert, L. Liensberger, M. Weiler, S. Wimmer, H. Ebert, and T. Kampfrath, High-throughput techniques for measuring the spin Hall effect, Phys. Rev. Appl. **14**, 064011 (2020).
[29] Y.-H. Zhu, B. Hillebrands, and H. C. Schneider, Signal propagation in time-dependent spin transport, Phys. Rev. B **78**, 054429 (2008).
[30] S. Kaltenborn, Y.-H. Zhu, and H. C. Schneider, Wave-diffusion theory of spin transport in metals after ultrashort-pulse excitation, Phys. Rev. B **85**, 235101 (2012).
[31] M. Battiato, K. Carva, and P. M. Oppeneer, Superdiffusive spin transport as a mechanism of ultrafast demagnetization, Phys. Rev. Lett. **105**, 027203 (2010).
[32] A. Melnikov, I. Razdolski, T. O. Wehling, E. Th. Papaioannou, V. Roddatis, P. Fumagalli, O. Aktsipetrov, A. I. Lichtenstein, and U. Bovensiepen, Ultrafast transport of laser-excited spin-polarized carriers in Au/Fe/MgO (001), Phys. Rev. Lett. **107**, 076601 (2011).
[33] R. Rouzegar *et al.*, Terahertz spin conductance probes of coherent and incoherent spin tunneling through MgO tunnel junctions, arXiv2305.09074.
[34] O. Gueckstock *et al.*, Terahertz spin-to-charge conversion by interfacial skew scattering in metallic bilayers, Adv. Mater. **33**, 2006281 (2021).
[35] C. Zhou *et al.*, Broadband terahertz generation via the interface inverse Rashba-Edelstein effect, Phys. Rev. Lett. **121**, 086801 (2018).
[36] M. B. Jungfleisch, Q. Zhang, W. Zhang, J. E. Pearson, R. D. Schaller, H. Wen, and A. Hoffmann, Control of terahertz emission by ultrafast spin-charge current conversion at Rashba interfaces, Phys. Rev. Lett. **120**, 207207 (2018).
[37] T. S. Seifert *et al.*, Terahertz spectroscopy for all-optical spintronic characterization of the spin-Hall-effect metals Pt, W and $Cu_{80}Ir_{20}$, J. Phys. D **51**, 364003 (2018).
[38] See Supplemental Material at http://link.aps.org/supplemental/10.1103/PhysRevLett.132.226703, which includes Refs. [39–48], for additional information about the spin current extraction (Note 1), sample preparation (Note 2), details about THz and optical spectroscopy (Note 3), error analysis (Note 4), spintronic origins of EO signals (Note 5), and the model of dynamical diffusion (Note 6).
[39] L. Braun, G. Mussler, A. Hruban, M. Konczykowski, T. Schumann, M. Wolf, M. Münzenberg, L. Perfetti, and T. Kampfrath, Ultrafast photocurrents at the surface of the three-dimensional topological insulator Bi_2Se_3, Nat. Commun. **7**, 13259 (2016).
[40] T. S. Seifert, S. Jaiswal, J. Barker, S. T. Weber, I. Razdolski, J. Cramer, O. Gueckstock, S. F. Maehrlein, L. Nadvornik, S. Watanabe *et al.*, Femtosecond formation dynamics of the spin Seebeck effect revealed by terahertz spectroscopy, Nat. Commun. **9**, 2899 (2018).
[41] J. Hui, H. Ma, Z. Wu, Z. Zhang, Y. Ren, H. Zhang, L. Zhang, and H. Wang, High-throughput investigation of crystal-to-glass transformation of Ti − Ni − Cu ternary alloy, Sci. Rep. **9**, 19932 (2019).
[42] K. Kawashima, Y. Okamoto, O. Annayev, N. Toyokura, R. Takahashi, M. Lippmaa, K. Itaka, Y. Suzuki, N. Matsuki, and H. Koinuma, Combinatorial screening of halide perovskite thin films and solar cells by mask-defined IR laser molecular beam epitaxy, Sci. Technol. Adv. Mater. **18**, 307 (2017).
[43] D. Wang, W. Jiang, S. Li, X. Yan, S. Wu, H. Qiu, S. Guo, and B. Zhu, A comprehensive review on combinatorial film via high-throughput techniques, Materials **16**, 6696 (2023).
[44] H. Xing, B. Zhao, Y. Wang, X. Zhang, Y. Ren, N. Yan, T. Gao, J. Li, L. Zhang, and H. Wang, Rapid construction of Fe − Co − Ni composition-phase map by combinatorial materials chip approach, ACS Comb. Sci. **20**, 127 (2018).
[45] N. C. Passler, M. Jeannin, and A. Paarmann, Layer-resolved absorption of light in arbitrarily anisotropic heterostructures, Phys. Rev. B **101**, 165425 (2020).
[46] P. Koleják, K. Postava, M. Mičica, P. Kužel, F. Kadlec, and J. Pištora, Experimental Gouy phase shift compensation in terahertz time-domain spectroscopy, Photonics Nanostruct. Fundam. Appl. **31**, 129 (2018).
[47] F. Lindner, G. G. Paulus, H. Walther, A. Baltuška, E. Goulielmakis, M. Lezius, and F. Krausz, Gouy phase shift for few-cycle laser pulses, Phys. Rev. Lett. **92**, 113001 (2004).
[48] T. Valet and A. Fert, Theory of the perpendicular magnetoresistance in magnetic multilayers, Phys. Rev. B **48**, 7099 (1993).
[49] P. Kubaščík *et al.*, Terahertz probing of anisotropic conductivity and morphology of CuMnAs epitaxial thin films, Adv. Phys. Res. **3**, 2300075 (2023).
[50] L. Nádvorník *et al.*, Broadband terahertz probes of anisotropic magnetoresistance disentangle extrinsic and intrinsic contributions, Phys. Rev. X **11**, 021030 (2021).
[51] T. S. Seifert *et al.*, Frequency-independent terahertz anomalous Hall effect in $DyCo_5$, $Co_{32}Fe_{68}$, and $Gd_{27}Fe_{73}$ thin films from DC to 40 THz, Adv. Mater. **33**, 2007398 (2021).
[52] N. W. Ashcroft and N. D. Mermin, *Solid State Physics* (Holt, Rinehart and Winston, New York, 1976).
[53] D. Gall, Electron mean free path in elemental metals, J. Appl. Phys. **119**, 085101 (2016).
[54] A. Leitenstorfer, S. Hunsche, J. Shah, M. C. Nuss, and W. H. Knox, Detectors and sources for ultrabroadband electro-optic sampling: Experiment and theory, Appl. Phys. Lett. **74**, 1516 (1999).
[55] T. Kampfrath, J. Nötzold, and M. Wolf, Sampling of broadband terahertz pulses with thick electro-optic crystals, Appl. Phys. Lett. **90**, 231113 (2007).
[56] J. Bass and W. P. Pratt, Spin-diffusion lengths in metals and alloys, and spin-flipping at metal/metal interfaces: An experimentalist's critical review, J. Phys. Condens. Matter **19**, 183201 (2007).
[57] J. Sinova, S. O. Valenzuela, J. Wunderlich, C. H. Back, and T. Jungwirth, Spin Hall effects, Rev. Mod. Phys. **87**, 1213 (2015).
[58] X. Shen, Y. Cai, Y. Wu, and Y. Ji, Tuning of spin relaxation and the Kondo effect in copper thin films by ionic gating, Phys. Rev. B **106**, 085118 (2022).

[59] E. Villamor, M. Isasa, L. E. Hueso, and F. Casanova, Contribution of defects to the spin relaxation in copper nanowires, Phys. Rev. B **87**, 094417 (2013).

[60] G. Li, R. V. Mikhaylovskiy, K. A. Grishunin, J. D. Costa, T. Rasing, and A. V. Kimel, Laser induced THz emission from femtosecond photocurrents in Co/ZnO/Pt and Co/Cu/Pt multilayers, J. Phys. D **51**, 134001 (2018).

[61] J. Bass and W. P. Pratt, Spin-diffusion lengths in metals and alloys, and spin-flipping at metal/metal interfaces: An experimentalist's critical review, J. Phys. Condens. Matter **19**, 183201 (2007).

[62] S. Maekawa, *Spin Current*, 1st ed. (Oxford University Press, Oxford, 2012).

[63] T. S. Seifert, D. Go, H. Hayashi, R. Rouzegar, F. Freimuth, K. Ando, Y. Mokrousov, and T. Kampfrath, Time-domain observation of ballistic orbital-angular-momentum currents with giant relaxation length in tungsten, Nat. Nanotechnol. **18**, 1132 (2023).